

Efficient Path Estimation through Parallel Media for Wide-Beam Ice-Sounding Radar

Álvaro Arenas-Pingarrón^{1*}, Paul V. Brennan¹, Hugh Corr²

¹ Department of Electronic and Electrical Engineering, University College London, Torrington Place, WC1E 7JE, London, United Kingdom

² British Antarctic Survey, High Cross, Madingley Road, CB3 0ET, Cambridge, United Kingdom

*E-mail: alvaro.pingarron.15@ucl.ac.uk

Abstract: We propose an algorithm to estimate the path followed by refracted signals from a source to a target, through a medium formed by uniform parallel layers with known different refractive indices, a common model used for ice radio-echo sounding. The analytical solution is a polynomial with a degree that exponentially depends on the number of layers, being computationally inefficient. For low incidence angles, the small-angle approximation can be used to avoid the polynomial. In our technique, we normalize the governing equations to obtain a framework where to find a narrow angular interval containing the solution, finally estimated interpolating the boundaries. The new approach improves the results regarding the small-angle approximation for a wider angular range at a slightly higher computational time. This method has been applied to focus airborne SAR images for deep ice sounding, reducing the calculation time and improving the detected response in wide-beam and squinted geometries, used for high along-track resolution or the detection of sloping internal layers.

1. Introduction

The elapsed travel time along the path followed by signals from a transmitter to a receiver is a key calculation in antenna arrays processing. In the case of a synthetic aperture radar (SAR), provided the propagation environment is known, the relative paths between the received signals in the channels of the array depend on the transmitter, target and receiver locations. These paths are the first step for calculating the range-azimuth reference functions, which in turn will be applied for cross-track beamforming, channel calibration, SAR focussing or direction of arrival (DoA) estimation algorithms.

When considering point-like sources and targets, the incidence angle of an electromagnetic (EM) wave through a half-spaced multilayer medium is obtained by ray tracing, with the equations defined by Snell's law and the ground distance between the source and the target. For the simplest case of two different uniform media, the exact incidence angle is found by solving the roots of a degree-4 polynomial [1], computationally time-demanding when processing 3D-distributed targets. For ice-sounding SAR imaging, where the path calculation is a bottle-neck during the processing, the small-angle approximation has been used [2-3], but it is inaccurate for large incidence angles, e.g. when a wide aperture is needed for high azimuth resolution, or for squinted processing (useful to detect the steep internal ice layers). Through-The-Wall Imaging (TRWI) [4] and Ground Penetrating Radar (GPR) [5] techniques can address the refraction mechanisms with the small-angle approximation, although in some applications the effect of refraction is neglected under the straight-ray approximation [6]. In fields where the layering is needed, other approaches have been applied, such as using a look-up table [7] followed by an interpolation. In ice-sounding applications, the convenience of at least two ice layers was put forward in [8], meaning for airborne systems a 12-th degree polynomial or a look-up table with at least 5 dimensions. In seismic analysis, the Dix's

approximation [9] estimates speeds and thicknesses of the different layers, using two sensors deployed on the surface in a bistatic configuration, measuring the propagation times varying the distance between the sensors. Conversely, Dix's equations allow to obtain the propagation time from a known environment and sensor locations.

This work is an extension of [10], for estimating the path from a source to a scatterer, given their locations and the environment, without data collected with the pertinent sensor. Its application is an initial step before processing the final products like radar images or DoA estimations. The details of the technique here presented are valid for an environment with arbitrary refractive indices in parallel media. The advantage of the last constrain is that the angle within a layer is invariant regardless its order of appearance, and hence it is possible to refer to a commutative property. With different interface slopes this property is no longer valid, adding degrees in the polynomial analytical solution. These environments are out of the scope of this paper, but their solution can be found with the strategy of the parallel media, after rotating the initial environment to obtain one, such that the overall effect of the slopes is counteracted, and hence the layers within the new system can be approximated as parallel. The rotation angle depends on the slope, thickness and refractive index of each layer.

In Section 2 is presented the environment model, following a section where the existing methods and their main properties are discussed. Section 4 develops the algorithm, firstly consisting in the normalization of parameters and equations [10], and secondly restricting the solution to be within close boundaries (detailed in this paper), before an iterative procedure [10], which at each step halves the interval length to converge to the solution. When the distance between boundaries is narrow enough according to the required accuracy, an interpolation can be made to get the final estimation. Approximations of the propagation time are also detailed. Section 5 includes the results and calculation time comparisons for different interval limits and interpolations,

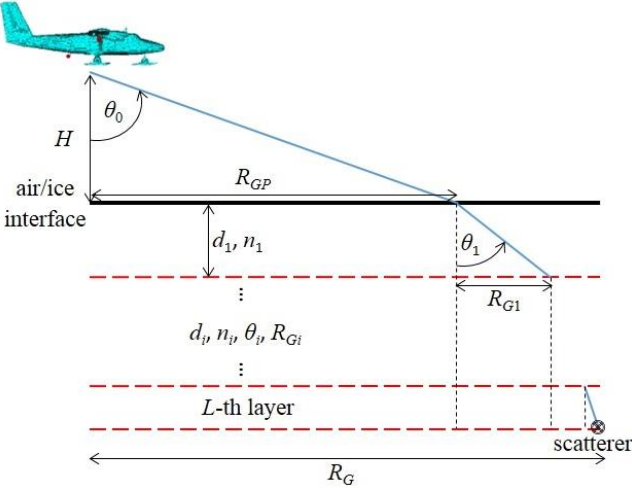


Fig. 1. Refraction path in a multilayer ice medium [10].

together with a range migration fitting of a SAR data take in Antarctica, collected with PASIN airborne radar by the British Antarctic Survey (BAS). The novelty of the present paper compared with [10] is to use small-angle approximations, among others, to efficiently achieve a tight initial interval and save iterations.

2. Parallel-layers model [10]

The speed of EM wave propagation varies inversely with refractive index and density of the medium. In ice, the wave propagation speed decreases with depth, since the air concentration reduces regarding the surface because of the precipitating snowflakes, and the ice becomes more compact due to higher pressure. In the shallowest ice layer, known as firn and which might extend down to about 150m depth, the propagation speed is higher, decreasing until a solid ice region, known as glacier ice, is reached, with an expected constant refractive index of about 1.78 [11], compared to a minimum value of about 1.20 for ice on surface [8].

Because the real estimation of the vertical-varying ice profile might be difficult, to simplify, a single uniform layer medium is considered, whereas a mean correction of around 10m is usually added for depth estimation, to account for the faster speed of propagation through firn [11]. Since refractive index increases with depth in the firn, a representative model should include discretized ice layers, as depicted in Fig. 1, where H is the radar height over the surface, R_G and R_{GP} are, respectively, the ground distances from radar to target and refraction point on surface, θ_0 the elevation angle in the source medium (air, for airborne SAR) and d_i , n_i , θ_i and R_{Gi} are, respectively, the thickness, the relative refractive index regarding the source medium ($n_0 = 1$), the incidence angle and the ground distance covered, of the i -th layer, out of L in which ice is divided.

The refraction path and elevation angle are calculated from the distance R_{GP} , as

$$\theta_0 = \tan^{-1} \left(\frac{R_{GP}}{H} \right). \quad (1)$$

In case the layers present identical slope but not perpendicular to the vertical, an equivalent environment can

be obtained by a rotation around the radar. The presented model, with pure refractions and a single backscattering or reflection, can also account for reflections on the internal interfaces, by adding as many extra layers as internal reflections and considering only refraction.

3. Previous methods

The direct application of Snell's law, i.e. a wave propagating through different media follows the fastest path, provides a polynomial for the exact solution. An approximation of Snell's law leads to small-angle (SA) calculations. As the equations to introduce these methods are the starting point for the contribution of the paper, they are reproduced from [10].

3.1. Exact polynomial solutions

Snell's law relates each layer i to the first medium (air) by

$$\sin \theta_0 = n_i \cdot \sin \theta_i, \quad 1 \leq i \leq L. \quad (2)$$

The ground distance R_G from source to target must be covered by the ground distances at each medium

$$R_{GP} + \sum_{i=1}^L R_{Gi} = R_G. \quad (3)$$

The case for the single-layer ice medium ($L = 1$) was solved in [1] as a degree-4 polynomial. The equation for the general case of L ice layers is [10]

$$\frac{d_1^2 R_{GP}^2}{P_1} = \left(R_G - R_{GP} - R_{GP} \cdot \sum_{i=2}^L \frac{d_i}{\sqrt{P_i}} \right)^2, \quad (4)$$

with P_i the degree-2 polynomial on R_{GP}

$$P_i(R_{GP}) = (n_i^2 - 1) R_{GP}^2 + n_i^2 H^2. \quad (5)$$

The degree of the polynomial (4) on R_{GP} is [10]

$$N = (L+1) \cdot 2^L, \quad (6)$$

what makes this technique computationally demanding.

3.2. Single small-angle approximation

Recalling from [10], an approximation for small angles can be applied [2], in which the sine of the incidence angles in free space and ice is approximated by the tangent. Rewriting (3) as

$$H \cdot \tan \theta_0 + \sum_{i=1}^L d_i \cdot \tan \theta_i = R_G \quad (7)$$

and approximating (2) by means of the tangents, it results

$$R_{GP} = H \cdot \tan \theta_0 \approx R_G \cdot \left(1 + \frac{1}{H} \cdot \sum_{i=1}^L \frac{d_i}{n_i} \right)^{-1}. \quad (8)$$

An alternative SA approximation is obtained substituting the sines and tangents in (2) and (7) directly by the angles, resulting θ_{0D} (label *D* for *direct*), in radians,

$$\theta_{0D} \approx R_G \cdot \left(H + \sum_{i=1}^L \frac{d_i}{n_i} \right)^{-1}. \quad (9)$$

called *direct* small-angle in this work. This method can lead to incidence angles greater than $\pi/2$ rad (90° , the limit according to Fig. 1), being a problem for shallow depths or large ground distances, and hence (8) is a more cautious estimation. Both offer fast analytical approaches. However, as the refraction paths are usually needed for elapsed time estimations from which to obtain phase measurements, its validity is finally wavelength dependent. Due to the small-angle constrain, specifically in SAR processing this approximation might be not valid for squinted geometries, high along-track resolutions or cross-track beamforming.

3.3. Dix's Method

This approach [9] estimates the propagation time, rather than the incidence angle, which can be calculated from the propagation time with a polynomial of degree (6). In the environment model of vertical variation, the estimation is based on a vector with vertical and horizontal propagation-time components, t_v and t_h , respectively. The vertical is calculated with the real propagation speed from the refractive indices n_i , whereas the horizontal requires an effective refractive index n_{hRMS} , as

$$n_{hRMS}^2 = \frac{H \cdot n_p + \sum_{i=1}^L d_i \cdot n_i}{H \cdot n_p^{-1} + \sum_{i=1}^L d_i \cdot n_i^{-1}}. \quad (10)$$

The horizontal speed covers the ground distance R_G . Hence, the Dix's estimated round-trip propagation time t_{DIX} is

$$t_{DIX} = \sqrt{t_h^2 + t_v^2} = \frac{2}{c_0} \sqrt{\left(R_G \cdot n_{hRMS} \right)^2 + \left(H \cdot n_p + \sum_{i=1}^L d_i \cdot n_i \right)^2}. \quad (11)$$

4. Development

Our method consists in delimiting an interval containing the solution, rather than directly obtaining a single point. The advantage of this technique is that it works for all angles, and the maximum error can be improved adding a recursive interval search. First, we introduce a normalized set of identities that represents the basis for all calculations and avoids trigonometric functions.

4.1. Development frame

Recalling from [10], with new variables x , y_i , a_i and b_i defined as

$$\begin{aligned} x &= \frac{H}{R_G} \tan \theta_0, & y_i &= \frac{d_i}{R_G} \tan \theta_i, \\ a_i &= \frac{d_i}{R_G \sqrt{(n_i^2 - 1)}}, & b_i &= \frac{n_i \cdot H}{R_G \sqrt{(n_i^2 - 1)}} \end{aligned} \quad (12)$$

$(x, y_i \in [0, 1])$, (7) is transformed into

$$x + \sum_{i=1}^L y_i = 1, \quad (13)$$

and the set of L equations in (2) into

$$y_i = \frac{a_i x}{\sqrt{b_i^2 + x^2}}, \quad 1 \leq i \leq L. \quad (14)$$

Clearing y_1 in (13) and with (14), it results

$$\begin{aligned} y_1 &= f_1(x) = 1 - x \cdot \left(1 + \sum_{i=2}^L \frac{a_i}{\sqrt{b_i^2 + x^2}} \right) \\ &= f_2(x) = \frac{a_1 x}{\sqrt{b_1^2 + x^2}}. \end{aligned} \quad (15)$$

The solution to the system is the crossing point x_c

$$x_c = \left\{ x \in [0, 1] \mid g(x) = f_1(x) - f_2(x) = 0 \right\} \quad (16a)$$

$$= \left\{ x \in [0, 1] \mid |g(x)| = |f_1(x) - f_2(x)| = 0 \right\} \quad (16b)$$

to finally obtain the ground distance from radar to surface as

$$R_{GP} = H \cdot \tan \theta_0 = x_c \cdot R_G. \quad (17)$$

In Fig. 2 [10] are plotted the functions in (15)-(16), for the case of $L = 2$, with radar at a ground distance of 300m and height of 500m, pointing a target within the glacier layer ($n_2 = 1.78$) 2km below the firn, the latter with a thickness $d_1 = 150$ m and $n_1 = 1.5$. Those points where y_1 is not within the interval $[0, 1]$ are not valid, since it would mean the EM wave refracts backwards (only possible in case the layers are not parallel), suggesting the interval where to find x_c can be reduced.

In case a look-up table is chosen for the path estimations, the normalization (12) of the layer thicknesses regarding R_G allows to reduce one dimension.

4.2. Interval limits

The unitary interval where to find the solution through (16) can be drastically reduced to facilitate the intersection

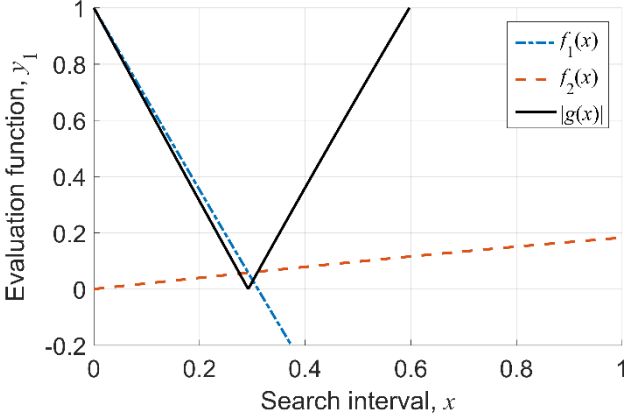


Fig. 2. Intersection point and evaluation curves (15)-(16) for $H = 500m$, $R_G = 300m$, $n_1 = 1.5$, $n_2 = 1.78$, $d_1 = 150m$ and $d_2 = 2km$ [10].

point search, saving the iterative steps otherwise needed to diminish the interval to an equivalent length.

The lowest and highest bounds will be found assuming a uniform medium made up by the minimum and maximum refractive indices, respectively. In the case of ice penetration with airborne radar, the lowest refractive index medium corresponds to the air, whereas the highest will be the deepest ice layer (not considering the likely reduction due to the warming bedrock). The case of a single uniform medium with the lowest refractive index and a total thickness equal to the sum of all media, provides a minimum incidence angle limit θ_{0um} in the radar medium (layer 0, label u for uniform, and m for minimum), since adding any layer with higher refractive index will bend the wave towards the direction perpendicular to the layers (all assumed to be parallel), and then, for covering a given ground range R_G , the incidence angle should be higher than this limit. With only one medium and a thickness sum of all media, the normalized variable x in (12) for θ_{0um} is, by geometry,

$$x_{um} = \frac{H}{R_G} \tan \theta_{0um} = \left(1 + \frac{1}{H} \sum_{i=1}^L d_i \right)^{-1}. \quad (18)$$

On the other hand, if a single medium filled with the highest refractive index and thickness equal to the sum of all media is considered, it allows to obtain a maximum incidence angle, because any lower refractive index will increase the aperture angle regarding the case of the assumed uniform medium. The highest angle θ_{LuM} (layer L , label u for uniform, and M for maximum) in the deepest medium will be

$$\tan \theta_{LuM} = \frac{R_G}{H + \sum_{i=1}^L d_i} = \tan \theta_{0um}, \quad (19)$$

with θ_{LuM} equal to θ_{0um} , since the geometries are the same. The angle θ_{LuM} is yet to be related to the air medium for calculating the boundaries of the solution x_c . The incidence angle in air medium will be obtained through the Snell's law

(2), which relates the tangent of angles in media i and j , without approximations, as

$$\begin{aligned} \tan \theta_i &= \tan \left(\arcsin \left(\left(n_j/n_i \right) \cdot \sin \theta_j \right) \right) \\ &= \frac{\left(n_j/n_i \right) \cdot \tan \theta_j}{\sqrt{1 + \left(1 - \left(n_j/n_i \right)^2 \right) \cdot \tan^2 \theta_j}}. \end{aligned} \quad (20)$$

In (20), setting $i = 0$ ($n_0 = 1$, by definition) and $j = L$ relates the angle in air medium θ_{0uM} to the angle θ_{LuM} in ice layer L . After (18) and (19) are used, the highest limit x_{uM} is

$$x_{uM} = \frac{H}{R_G} \tan \theta_{0uM} = \frac{n_L \cdot x_{um}}{\sqrt{1 + \left(1 - n_L^2 \right) \left(\frac{R_G}{H} \right)^2 x_{um}^2}} \quad (21)$$

The interval length can be further reduced with the SA approximation (8), where the sinus of an angle was approximated to its tangent. For angles θ_i and θ_j , after the Snell's law, θ_j and its approximation $\tilde{\theta}_j$ take the form

$$\tan \theta_j = \tan \left(\arcsin \left(\left(n_i/n_j \right) \cdot \sin \theta_i \right) \right), \quad (22a)$$

$$\tan \tilde{\theta}_j = \left(n_i/n_j \right) \cdot \tan \theta_i. \quad (22b)$$

Equation (22a) can be developed as

$$\tan \theta_j = \frac{\left(n_i/n_j \right) \cdot \sin \theta_i}{\sqrt{1 - \left(n_i/n_j \right)^2 \cdot \sin^2 \theta_i}}, \quad (23)$$

leading to two cases according to the refractive indices,

$$n_j \geq n_i \Rightarrow \tan \theta_j \leq \frac{\left(n_i/n_j \right) \cdot \sin \theta_i}{\sqrt{1 - \sin^2 \theta_i}} = \tan \tilde{\theta}_j, \quad (24a)$$

$$n_j \leq n_i \Rightarrow \tan \theta_j \geq \frac{\left(n_i/n_j \right) \cdot \sin \theta_i}{\sqrt{1 - \sin^2 \theta_i}} = \tan \tilde{\theta}_j. \quad (24b)$$

(24a) means that the SA approximation $\tilde{\theta}_j$ in medium j , using as reference the medium i , is an overestimation of the real angle θ_j ($\tilde{\theta}_j \geq \theta_j$) when the reference medium has a lower refractive index, whereas (24b) points out an underestimation ($\tilde{\theta}_j \leq \theta_j$) when the refractive index in the reference medium is higher. If the medium with lowest refractive index is taken as the reference ($i=0$, the air for airborne radar application), and (22b) is used for approximating θ_j with $\tilde{\theta}_j$ through θ_0 , these approximations are an overestimation of the real angles, and when included in (7) the resulting horizontal distance from radar to target is longer than R_G ,

$$H \cdot \tan \theta_0 + \sum_{i=1}^L \frac{d_i}{n_i} \cdot \tan \theta_0 \geq R_G ,$$

$$\tan \theta_0 \geq R_G \cdot \left(H + \sum_{i=1}^L \frac{d_i}{n_i} \right)^{-1} = \tan \theta_{0sm} , \quad (25)$$

what defines a new lower limit angle θ_{0sm} in the air medium, with the corresponding inferior limit for the search interval x_{sm} (label *s* for SA, and *m* for minimum)

$$x_{sm} = \frac{H}{R_G} \tan \theta_{0sm}$$

$$= \left(1 + \frac{1}{H} \sum_{i=1}^L \frac{d_i}{n_i} \right)^{-1} \leq \frac{H}{R_G} \tan \theta_0 = x_c . \quad (26)$$

This inferior limit is greater than x_{um} in (18), since $n_i \geq 1$, fact assumed choosing as the reference medium the one with lowest refractive index (n_0). In Fig. 3(a) is included this situation, for $L=2$ and refractive index increasing with the depth. The solid trajectory represents the real path, whereas the dotted one approximates the angles $\tilde{\theta}_1$ and $\tilde{\theta}_2$ in ice by the overestimation (24a), and has an incidence angle in air equal to the real path, because it is the reference layer. The dashed path represents the angle θ_{0sm} , lower than θ_0 to compensate the horizontal distance excess $E_0 > 0$ due to the overestimations.

Similarly, if the reference medium is the one with the highest refractive index (in ice-sounding the deepest layer, with index L), the angles for the rest of the layers are underestimated, and thus for covering R_G the angle θ_{Lsm} in the reference medium is larger than θ_L . Using (22b) in (7) for approximating θ_j with $\tilde{\theta}_j$ through θ_L

$$H \cdot n_L \tan \theta_L + \sum_{i=1}^L d_i \frac{n_L}{n_i} \tan \theta_L \leq R_G ,$$

$$\tan \theta_L \leq \frac{R_G}{H \cdot n_L + \sum_{i=1}^L d_i \frac{n_L}{n_i}} = \frac{R_G}{H} \frac{x_{sm}}{n_L} = \tan \theta_{Lsm} . \quad (27)$$

After converting θ_{Lsm} in (27) to an angle θ_{0sm} in the air medium by means of (20), a new maximum x_{sm} is found

$$x_{sm} = \frac{H}{R_G} \tan \theta_{0sm}$$

$$= \frac{x_{sm}}{\sqrt{1 - \left(1 - \frac{1}{n_L^2} \right) \left(\frac{R_G}{H} \right)^2 x_{sm}^2}} = \frac{x_{sm}}{\sqrt{1 - \frac{x_{sm}^2}{b_L^2}}} , \quad (28)$$

lower than x_{um} in (21), because the corresponding angle θ_{Lsm} (27) in layer L is also lower than θ_{LuM} (19). In Fig. 3(b) is represented the $L=2$ case for θ_{0sm} , with the solid trajectory being the real path (equal to the solid path in Fig. 3(a)), the dotted lines the approximated with the underestimated angles $\tilde{\theta}_0$ and $\tilde{\theta}_1$ (24b), and the dashed path the case of θ_{0sm} (from

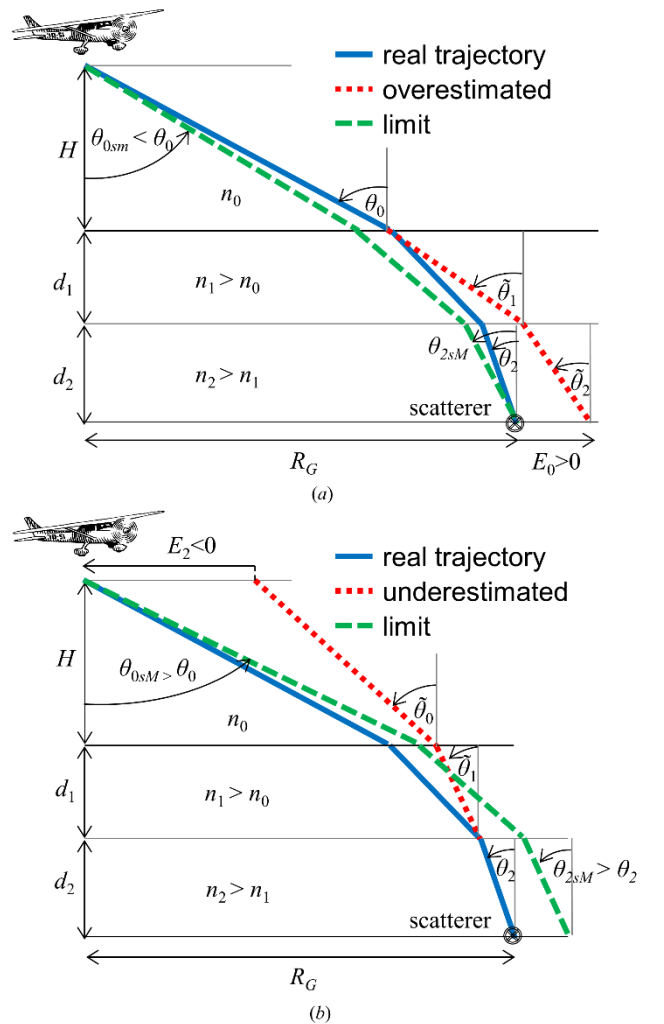


Fig. 3. Boundary angles with small-angle approximations.
(a) Lower limit θ_{0sm} , with layer 0 as reference.
(b) Upper limit θ_{0sm} , with layer 2 as reference.

θ_{2sm}), greater than θ_0 to compensate the horizontal distance lack $E_2 < 0$.

The limits x_{sm} and x_{sm} use the SA approximation with the reference layers of minimum and maximum refractive index, respectively, to ensure the over- and underestimation of the angles in the rest of layers. In general, if more than two layers are considered (i.e. more than a single ice layer in airborne ice sounding), tighter boundaries can be found with other layers. If for every layer is measured the excess or lack of the ground range travelled due to the corresponding SA approximation, those layers with the least excess or lack are finally chosen as references. For a reference layer with index ref , the difference E_{ref} between the horizontal distances covered by the approximated angles $\tilde{\theta}_i$ and the real ones θ_i is

$$E_{ref} = \sum_{i=0}^L d_i \cdot (\tan \tilde{\theta}_i - \tan \theta_i) . \quad (29)$$

By means of the $\tilde{\theta}_i$ SA approximation using θ_{ref} in (22b), the Snell's law in terms of the tangents in (20) for relating θ_i and θ_{ref} to θ_0 , and renaming the height H as d_0 , the excess is

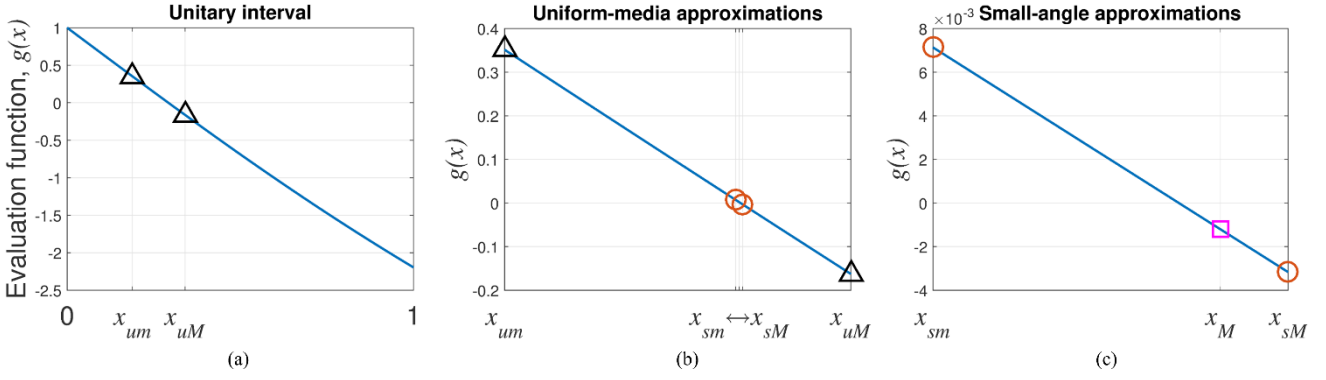


Fig. 4. Evaluation function $g(x)$ and interval limits of Table 1, for the environment of Fig. 2.

(a) Boundaries from the uniform-media approximation (triangles). (b) Small-angle approximations (circles) using air medium and the deepest layer as references. (c) Improvement (square) of upper limit with firn layer as reference.

$$\begin{aligned} E_{ref} &= n_{ref} \cdot \tan \theta_{ref} \cdot \left(\sum_{i=0}^L \frac{d_i}{n_i} \right) - \sum_{i=0}^L d_i \cdot \tan \theta_i \\ &= \tan \theta_0 \cdot \left(\frac{S_1}{\sqrt{1 + \left(1 - \left(1/n_{ref}\right)^2\right) \tan^2 \theta_0}} - S_2 \right), \end{aligned} \quad (30)$$

with S_1 and S_2 independent of the reference layer ref , as

$$\begin{aligned} S_1 &= \sum_{i=0}^L \frac{d_i}{n_i}, \\ S_2 &= \sum_{i=0}^L \frac{d_i}{n_i} \cdot \left(1 + \left(1 - \frac{1}{n_i^2} \right) \tan^2 \theta_0 \right)^{-1/2}. \end{aligned} \quad (31)$$

(30) is positive when the horizontal distance is greater than R_G and negative when it is lower. θ_0 can be approximated by the mean of the limits x_{sm} and x_{sM}

$$\tan \theta_0 = \frac{R_G}{H} x_c \approx \frac{R_G}{H} \cdot \frac{(x_{sm} + x_{sM})}{2}. \quad (32)$$

Since the only interest of (30) is the qualitative positive or negative value, it is convenient to obtain the reference refractive index that gives zero excess, n_z , as

$$n_z = \left(1 + \frac{1 - (S_1/S_2)^2}{\tan^2 \theta_0} \right)^{-1}. \quad (33)$$

The layer m with a refractive index n_m closest from below to n_z , will be the reference with the minimum positive excess E_m , allowing the infimum of the interval (the maximum lower limit, x_m). Similarly, the layer M with a refractive index n_M closest from above to n_z , with maximum negative excess E_M , gets the supremum (the minimum upper limit, x_M).

$$m = i \in \{0, \dots, L\} \mid \forall ref \in \{0, \dots, L\}, 0 \leq E_i \leq E_{ref}, \quad (34a)$$

Table 1. Interval limits, in increasing order, and solution x_c .

limit	x_{um}	x_{sm}	x_m	x_c	x_M	x_{sM}	x_{uM}
eq.	(18)	(26)	(35a)	(16a)	(35b)	(28)	(21)

$$M = i \in \{0, \dots, L\} \mid \forall ref \in \{0, \dots, L\}, E_{ref} \leq E_i \leq 0. \quad (34b)$$

The corresponding limits x_m and x_M will be obtained following a development like (27)-(28), with

$$x_m = \frac{x_{sm}}{\sqrt{1 - \left(1 - \frac{1}{n_m^2}\right) \left(\frac{R_G}{H}\right)^2 x_{sm}^2}} = \frac{x_{sm}}{\sqrt{1 - \frac{x_{sm}^2}{b_m^2}}}, \quad (35a)$$

$$x_M = \frac{x_{sM}}{\sqrt{1 - \frac{x_{sM}^2}{b_M^2}}}. \quad (35b)$$

For ice-sounding with an increasing refractive index, E_{ref} will decrease as the layer under test is deeper located. Thus, a strategy to avoid the calculation of all the excesses is to start with the shallowest ice layer (as the air has the lowest refractive index), and the first with negative E_{ref} will be the one for obtaining the maximum, whereas the layer above, the best for the minimum, so that $m = M - 1$. A summary of the limits in increasing order and their equations is in Table 1.

In Fig. 4 is plotted the evaluation function against the points x within the search intervals, together with the boundaries of Table 1, using the same parameters as in Fig. 2. The solution of the system is the point where $g(x) = 0$. The initial unitary interval in abscises is in Fig. 4(a), where the uniform-media approximations (triangles) give $x_{um} \approx 189 \times 10^{-3}$ with the air medium (lowest refractive index), and $x_{uM} \approx 341 \times 10^{-3}$ with the deepest layer (highest refractive index). Fig. 4(b) is limited to the previous intervals, and includes the SA approximations using the air and the deepest ice layer (circles), giving the limits $x_{sm} \approx 290.1 \times 10^{-3}$ and $x_{sM} \approx 293.1 \times 10^{-3}$. The latter is improved by the firn ($n_1 = 1.5$) as reference, satisfying the condition (34b) for a supremum $x_M \approx 292.6 \times 10^{-3}$ (square mark in Fig. 4(c)).

Because when the layers are parallel they are commutative from the point of view of the elapsed time along

the path, with an arbitrary distribution of refractive indices, the algorithm must sort the layers in ascending refractive index to fast converge to the optimal interval search.

4.3. Solution search algorithms

Since $f_1(x)$ and $f_2(x)$ in (15) are respectively strictly monotonically decreasing and increasing, the solution $g(x)=0$ is unique, what enables to apply an optimized algorithm to find the solution by means of $g(x)$, with zero-crossing, or $|g(x)|$, with the minimum. The ‘Bisection’ method [12], based on the divide-and-conquer technique, was used to calculate (16), halving the interval according to the sign of $g(x)$.

The number of iterations determines the maximum error in the abscise interval $[0, 1]$: as the ratio of the interval length after consecutive iterations is 2, after K steps the ratio is 2^{K+1} (for $K=0$ the point 0.5 would be taken as the solution), and thus an error of $2^{-(K+1)}$ occurs [10].

The iterative search of minimum or crossing point, as it approximates to the solution, can be regarded as a method to set better infimum and supremum limits than those in section 4.2 (see Table 1). Also, for a given number of iterations, the boundaries previously explained may offer a narrow interval. For example, with the environment defined for Fig. 2 and Fig. 4, the interval length due to the uniform-media approximation is $\Delta x_u = x_{uM} - x_{um} \approx 152 \times 10^{-3}$, whereas after the SA approximations is $\Delta x_s = x_M - x_{sm} \approx 2.5 \times 10^{-3}$. Because each iteration divides the search interval by 2, the interval length is 2^{-K} , and the algorithm needs 3 iterations ($\Delta = 125 \times 10^{-3}$) to improve the uniform media approximation, and 9 ($\Delta = 1.95 \times 10^{-3}$) for beating the SA interval. The equivalent number of iterations (ENI), defined as the number of iterations needed to obtain an interval equal to the limits distance,

$$ENI = -\log_2 \Delta x, \quad (36)$$

allows to compare the performances of the interval limits and the iterative procedures.

4.4. Solution interpolation

A linear interpolation of $g(x)$ in (16a) within an interval improves the estimation of x_c , offering better resolution than several further iterative steps. With lower and upper boundaries x_- and x_+ , and approximating the slope of $g(x)$ within the boundaries as $g'(x_c) \approx (g(x_+) - g(x_-)) / (x_+ - x_-)$, the estimated solution is

$$x_c \approx x_- - \frac{g(x_-)}{g'(x_c)} = x_- + \frac{x_+ - x_-}{1 - g(x_+)/g(x_-)}. \quad (37)$$

Following with the example plotted in Fig. 2 and Fig. 4, the infimum and supremum are $x_- = x_{sm}$ and $x_+ = x_M$, with $g(x_-) = 7.1 \times 10^{-3}$ and $g(x_+) = -1.2 \times 10^{-3}$, resulting in $x_c \approx 292.2 \times 10^{-3}$.

Since the absolute value of the slope of function $g(x)$ decreases with x , the linear interpolation is always an overestimation of the solution, what may justify the use of a quadratic interpolator. Because the interpolated value is a better approach than (32), it improves the estimation of n_z (33), although in practice a recalculation is not needed.

4.5. Sensitivity analysis

The solutions after the mean and linear interpolations offer analytical approaches in a close form, for analysis that with the polynomial forms cannot be easily performed, like the relative sensitivity to depth and refractive index. This measurement is defined as the ratio of the *relative* variation in parameter v to the *relative* variation in u , and is given by

$${}^v_u S = \lim_{\substack{\Delta v \rightarrow 0 \\ \Delta u \rightarrow 0}} \left(\frac{\Delta v}{v} \right) \left/ \left(\frac{\Delta u}{u} \right) \right. = \left(\frac{\partial v}{\partial u} \right) \cdot \frac{u}{v}. \quad (38)$$

With $L=2$, for a scatterer located at fixed depth d_B , the SA lower bound limit x_{sm} is (26)

$$x_{sm} = \left(1 + \frac{1}{H} \cdot \left(\frac{d_1}{n_1} + \frac{d_B - d_1}{n_2} \right) \right)^{-1}, \quad (39)$$

with sensitivities to thickness d_1 and refractive index n_1 of the firn layer as, respectively,

$${}_{d_1}^x S = -1 + \left(1 + \left(\frac{n_2 / n_1 - 1}{d_B + n_2 H} \right) \cdot d_1 \right)^{-1} \leq 0, \quad (40)$$

$${}_{n_1}^x S = \left(1 + \left(\frac{H}{d_1} + \frac{1}{n_2} \left(\frac{d_B}{d_1} - 1 \right) \right) \cdot n_1 \right)^{-1} \geq 0, \quad (41)$$

the former improving (closer to zero) when the refractive index of the firn approaches that of the glacial layer (n_2), and the latter when the firn is narrow compared to the total thickness d_B . The sensitivity for the upper bound x_{sm} is obtained from the chain rule

$${}^w_u S = \frac{\partial w}{\partial u} \cdot \frac{u}{w} = \frac{\partial w}{\partial v} \cdot \frac{\partial v}{\partial u} \cdot \frac{v}{w} \cdot \frac{u}{v} = {}^w_v S \cdot {}^v_u S, \quad (42)$$

using (28) and (40), resulting in

$${}_{d_1}^{x_c} S = \frac{{}_{x_{sm}}^{x_{sm}} S \cdot {}_{d_1}^{x_{sm}} S}{1 - \frac{x_{sm}^2}{b_2^2}}^{-1} \cdot {}_{d_1}^{x_{sm}} S \geq {}_{d_1}^{x_{sm}} S, \quad (43)$$

and analogous for the sensitivity regarding n_1 . Finally, the sensitivity of the mean interpolation (32) is

$${}_{d_1}^{x_c} S = \frac{{}_{x_{sm}}^{x_{sm}} S \cdot (1 - \Gamma)}{1 - \frac{x_{sm}^2}{b_2^2}} + \frac{{}_{x_{sm}}^{x_{sm}} S \cdot \Gamma}{1 - \frac{x_{sm}^2}{b_2^2}}, \quad (44)$$

with

$$\Gamma = \frac{x_{sm}}{x_{sm} + x_{sm}}, \quad (45)$$

and similarly for the sensitivity regarding n_1 .

4.6. Propagation time

Most radar applications require the travelling time for data processing, being the traced path an intermediate step. Dix's equations (11) estimate directly the propagation time, saving the calculation of the incidence angle. With the incidence angle θ_0 of the initial layer and the subsequent θ_i from the Snell' law (2), the exact propagation time t_{SNELL} is

$$t_{SNELL} = \frac{2}{c_0} \left(\frac{H}{\cos \theta_0} + \sum_{i=1}^L d_i n_i \right) \\ = \frac{2}{c_0} \left(\frac{H}{\cos \theta_0} + \sum_{i=1}^L d_i n_i \left(1 - \left(\frac{\sin \theta_0}{n_i} \right)^2 \right)^{-1/2} \right). \quad (46)$$

Any approximation of the incidence angle in first layer with $\tilde{\theta}_0$, and in next layers after Snell's law with $\tilde{\theta}_i$, will lead to an error if applying (46), because the EM trajectory will not reach the scatterer. However, the trajectory with the small-angle (SA) does impinge on the scatterer (Fig. 3(a), with dashed trajectory), although the initial incidence angle is worse than other approximations with (32) or (37). This suggests the travelling time with SA could be more accurate than using a more precise incidence angle together with the Snell's law. From the exact expression (46), using $\cos^2 \theta = 1 + \tan^2 \theta$, with the initial incidence angle θ_{0sm} from SA and the SA approximations (22b) for the rest of layers, the propagation time is t_{SA} (referred as *pure* SA)

$$t_{SA} = \frac{2}{c_0} \left(H \sqrt{1 + \tan^2 \theta_{0sm}} + \sum_{i=1}^L d_i n_i \sqrt{1 + \frac{\tan^2 \theta_{0sm}}{n_i^2}} \right). \quad (47)$$

The propagation time improves if for the initial layer the travelling time and ground distance are solved with an accurate incidence angle, whereas the remaining time and distances are accounted for with the SA approximations. With the initial incidence angle $\tilde{\theta}_0$ and the corresponding normalized solution \tilde{x}_c , the residual ground distance R'_G is

$$R'_G = R_G - H \tan \tilde{\theta}_0 = R_G - R_G \tilde{x}_c = R_G \cdot (1 - \tilde{x}_c). \quad (48)$$

After removing the first layer, the SA approximation for the second layer ($i=1$) results in the incidence angle θ'_{1sm}

$$\tan \theta'_{1sm} = R'_G \cdot \left(d_1 + n_1 \sum_{i=2}^L \frac{d_i}{n_i} \right)^{-1} = \frac{R_G}{n_1 H} \frac{(1 - \tilde{x}_c) x_{sm}}{1 - x_{sm}}. \quad (49)$$

Hence, a better approximation \tilde{t} of the total propagation time is the summation of the travelling times of, first, the initial layer with an accurate incidence angle, and second, the rest of layers with SA estimations:

$$\tilde{t} = \frac{2}{c_0} \left(\sqrt{H^2 + R_G^2 \tilde{x}_c^2} + \sum_{i=1}^L d_i n_i \sqrt{1 + \frac{n_1^2}{n_i^2} \tan^2 \theta'_{1sm}} \right). \quad (50)$$

5. Results and comparisons

Fig. 5 displays the errors of the incidence angles and propagation times. The errors are calculated by subtracting to the estimations the expected values, the latter obtained with the polynomial solution for the upper incidence angle and Snell's law for the rest of layers. The model parameters are the same as for Fig. 2, except for the ground distance R_G , now from 0 to 1640m. Because there are $L=2$ ice layers, the polynomial solution is of degree-12 (6). Fig. 5(a) shows the errors of the incidence angle θ_0 (deg) at the air-ice interface, for the single SA (dashed) (26), direct SA (dashed-dotted) (9), SA intervals followed by mean (dotted) (32) and linear interpolation (solid) (37) techniques. The error increases with the ground distance, being higher for the single SA methods, improved by the mean of the interval limits, and significantly reduced after a linear interpolation. Due to the scatterer depth and R_G , the direct SA presents a lower absolute error than with x_{sm} . The propagation time errors (ns) against the expected incidence angles (deg) are shown in Fig. 5(b): Dix's method (solid black) (11); exact with Snell's law t_{SNELL} (46), starting with incidence angles from single SA (thin dashed) and SA with linear interpolation (thin solid yellow); pure SA approximation t_{SA} (47), starting from single SA (thick dashed); and travelling times \tilde{t} (50), starting from SA with mean (thick dotted) and linear (thick solid yellow) interpolations. For a given error limit in the propagation time, after comparing t_{SNELL} from the linear SA interpolation with pure t_{SA} , the maximum incidence angle is improved in the former by only 3°, which might not justify its higher computational effort of (37). The error slope for pure t_{SA} is lower than for t_{SNELL} from the linear SA interpolation, with errors crossing at 40° with 15ns (not displayed in Fig. 5(b)). At 50° incidence angle, the errors of t_{SA} and t_{SNELL} are 58ns and 116ns, respectively. However, the travelling times with \tilde{t} (50) greatly improve the maximum incidence angle in more than 20° regarding t_{SA} , even with the mean SA interpolation (32) as starting incidence angle.

The order of complexity of the polynomial solutions for L ice layers is $O(L^2 2^{2L})$ [10]. The single SA approximation has an order $O(L)$, and during the iterative part, for K iterations, the complexity is $O(K \cdot L)$ [10]. The calculation of the greater bound needs an extra root square (21), (28) to be added to the single SA approximation. The evaluation function has also a linear order, but it requires the calculations of root squares according to L (15). The time consumption for a single angle calculation is in Fig. 6, for the same cases as Fig. 5(a). The horizontal axis represents the ENI, to compare the interpolation methods against the method with only iterations. As the ENI value is not applied for the SA approaches (dashed) they have a constant consumption time, lower for the direct SA (dot-dashed) (9) than for SA with x_{sm} (dashed, crosses) (26), because the former does not calculate the inverse of the tangent. For the cases of mean (dotted) and linear interpolation (solid), the time is constant until an ENI of 9, meaning the interval reduction is equivalent to 9 iterations. If the requirements of the angle calculation are beyond this number, the iterative method must start from the reduced interval limits, linearly increasing the time. The

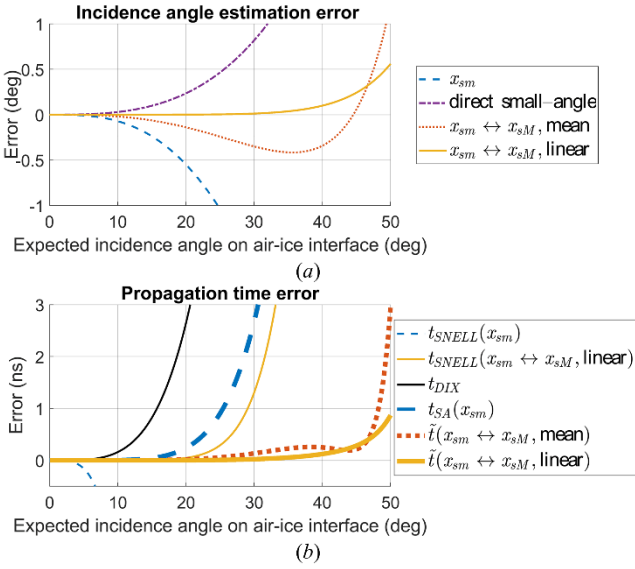


Fig. 5. Path errors regarding the expected angles, for the same parameters as in Fig. 2, with R_G from 0 to 1640m.
(a) Incidence angle error (deg), on air-ice interface.
(b) Propagation time error (ns).

difference between the mean and linear methods is that the latter needs the evaluation (16a) of the lower and greater interval limits: since each iteration means the evaluation of a point, the time difference between mean and linear interpolations up to 9 ENI is comparable to two iteration steps plus extra time for the calculation of parameters in (12). For higher ENI, the difference is reduced and kept constant, as the mean interpolation now requires a single evaluation for each new step, whereas the linear reuses one evaluation point from the last iteration. The polynomial solution ($L=2$, degree-12) took $\sim 50\mu\text{s}$, whereas neglecting the firn layer ($L=1$, degree-4) resulted in $\sim 15\mu\text{s}$.

Fig. 7, adapted from [10], shows the range(vertical, samples)-Doppler(horizontal, Hz) SAR response (dB, normalised) of an approximately flat bedrock at 3.4km depth, assuming the main detected responses are from scatterers below radar trajectory. The Doppler domain is calculated with the Fourier Transform. The data were taken above Recovery Glacier, using the British Antarctic Survey PASIN (Polarimetric Airborne Scientific Instrument) airborne SAR at 150MHz, with height above surface 340m, speed 55.2m/s, pulse repetition frequency 156.25Hz and sampling frequency 24MHz. Superimposed on the image are the expected footprints after estimating the paths with the refraction model, and the consequent range and Doppler frequency corresponding to each radar location. Assuming a uniform ice-layer ($L=1$) with thickness 3.4km and refractive index 1.78, the incidence angles are estimated with the single SA approximation (26) (dashed), the single direct SA (9) (dotted), SA interval with mean (32) (dot-dashed) and linear (37) (solid) interpolations, and pure iterative method after 17 steps (thin, dot-dashed). If the first $d_1 = 100\text{m}$ are considered as a new layer (firn) with refractive index $n_1 = 1.3$, the expected bed is 27m deeper than for $L=1$. The propagation time is estimated with the Snell's law (46). The thin solid line, corresponds to this case ($L=2$) with the pure iterative method, after 17 steps. On the top axis, the corresponding incidence angle in air medium has been included, equivalent to the along-track

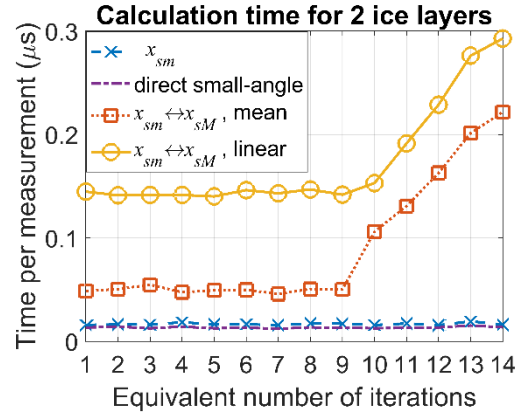


Fig. 6. Calculation time of a single incidence angle, for the same parameters and estimation methods as in Fig. 5.

look-angle for nadir geometry, related to the Doppler frequencies f_d by

$$f_d = \frac{2v}{\lambda_0} \sin \theta_0, \quad (51)$$

with λ_0 the wavelength in air medium and v the aircraft speed. All estimations match the curvature obtained from the radar data for vertical incidence angles. For oblique angles, the SA approximations with single values and mean interpolation clearly divers from the iterative estimation, expected to be accurate after 17 steps. As seen in the positive Doppler frequency branch (with stronger response than the negative), the SA mean interpolation is the solution that better fits the detected response, but as this is not the most accurate path estimation given a model, this best fit occurs because the current model should be modified, like for example with off-nadir backscattering (not below aircraft trajectory) or with sloping internal ice layers. The SA linear interpolation almost overlaps with the iterative case, the latter with negligible error provided a model. The iterative cases for $L=1$ and $L=2$ ice layers also almost overlap, because when $L=2$ the firn layer of 100m is very narrow compared to the glacial layer of 3.327km (for a total ice thickness of 3.427km, against the 3.4km when $L=1$), in agreement with the sensitivity analysis in (40) and (41). For shallow scatterers, for example when the main interest are the internal ice layers, or for other applications like mine detection, the significance of upper layers is greater, and hence they should be considered.

The wavelength analysis has not been included in this work, but depending on it, the environment model and the approximations carried out might be invalid, needing more layers or accuracy in the estimation, the shorter the wavelength. For PASIN, with 150MHz, the error of 1ns in Fig. 5(b) equals to a phase error of 54° . The sensitivity of PASIN allows a depth detection of 5km, but it finally depends on the ice column properties, such as ice type, internal crevasses and bottom interface.

6. Conclusions

The proposed approach allows a fast estimation of signal paths when travelling across a stratified medium made up of parallel layers, delimiting the solution by small-angle

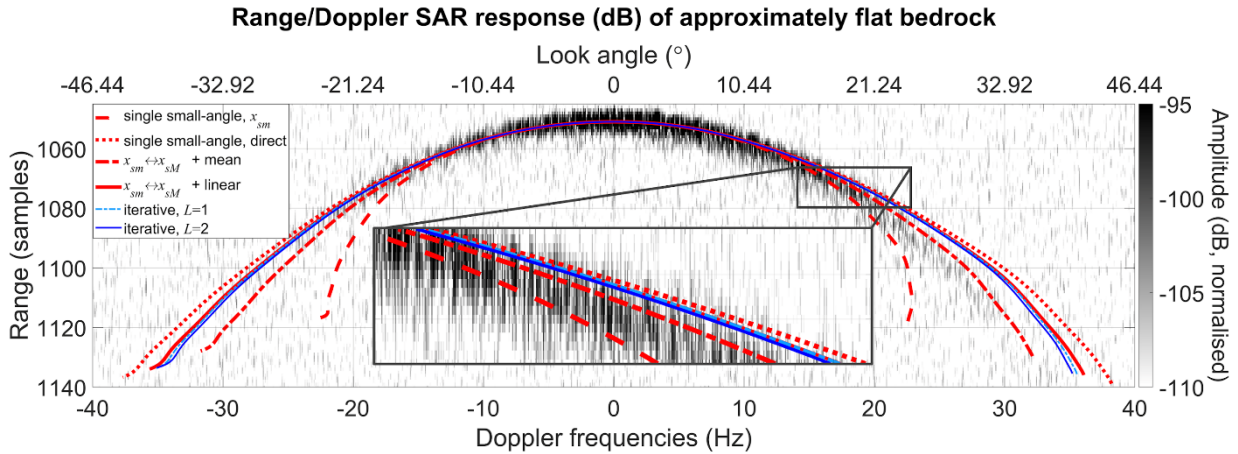


Fig. 7. Path estimation results, superimposed to the range(vertical)-Doppler(bottom) SAR response (dB, normalised) of bedrock calculated with a Fourier Transform, and the along-track incidence look-angle (top), adapted from [10]. Radar data were collected with PASIN, an airborne SAR. The range-Doppler footprint was estimated using the propagation delay from the refraction angles.

approximations, and when needed, applying any of the well-known minimum search algorithms based on iteration. Finally, an interpolation can be performed to reduce the error. Its efficiency can be improved processing each layer with parallel computing, for initially obtaining the smallest interval around the solution and also during the iterating stage. Although this work is framed in ice-sounding, it can be applied to other fields, with environments which have parallel layers and arbitrary refractive indices, and in particular to soil-sounding for mine and water detection, atmospheric radars or radar through-the-wall. The next step will be the development of an algorithm to take into account non-parallel layers, using the same strategies here presented.

7. Acknowledgments

We thank C.N. Robinson and R.J. Bullock for the collection and processing of raw data, and L.B. Lok and K. Nicholls for the suggestions and reviews.

This work was supported by the Natural Environment Research Council (NERC) [grant reference NE/L013444/1].

8. References

- [1] Hélière, F., Lin, C.-C., Corr, H., et al.: ‘Radio echo sounding of Pine Island Glacier, West Antarctica: aperture synthesis processing and analysis of feasibility from space’, IEEE Trans. Geosci. Remote Sens., 2007, 45, (8), pp. 2573–2582.
- [2] Kusk, A., Dall, J.: ‘SAR focusing of P-band ice sounding data using back-projection’. Proc. 2010 IEEE Int. Geosci. and Remote Sens. Symp., Honolulu, HI, USA, July 2010, pp. 4071–4074.
- [3] Legarsky, J. J., Gogineni, S. P., Akins T. L.: ‘Focused synthetic aperture radar processing of ice-sounder data collected over the Greenland Ice Sheet’, IEEE Trans. Geosci. Remote Sens., 2001, 39, (10), pp. 2109–2117.
- [4] Ahmad, F., Amin, M. G., Kassam, S. A.: ‘Synthetic aperture beamformer for imaging through a dielectric wall’, IEEE Trans. Aerosp. Electron. Syst., 2005, 41, (1), pp. 271–283.
- [5] Garcia-Fernandez, M., Morgenthaler, A., Alvarez-Lopez, Y., et al.: ‘Bistatic Landmine and IED Detection Combining Vehicle and Drone Mounted GPR Sensors’, Remote Sens., 2019, 11, (19), 2299.
- [6] Fioranelli, F., Salous, S., Ndip, I., et al.: ‘Through-The-Wall Detection With Gated FMCW Signals Using Optimized Patch-Like and Vivaldi Antennas’, IEEE Trans. Antennas and Propag., 2015, 63, (3), pp. 1106–1117.
- [7] Newman, T.: ‘Application of synthetic aperture techniques to radar echo soundings of the Pine Island Glacier, Antarctica’. PhD thesis, University College London, 2011.
- [8] Rasmussen, L. A.: ‘Refraction Correction for radio echo-sounding of ice overlain by firn’, J. Glaciol., 1986, 32, (111), pp. 193–194.
- [9] McGrath, D., Sass, L., O’Neil, S., et al: ‘End-of-winter snow depth variability on glaciers in Alaska’, J. Geophys. Res. Earth Surf.’, 2015, 120, (8), pp. 1530–1550.
- [10] Arenas-Pingarrón, A., Brennan, P. V., Corr, H.: ‘Refraction angle calculation in multilayered ice for wide-beam airborne radar’. Proc. 2018 IEEE Int. Geosci. and Remote Sens. Symp., Valencia, Spain, July 2018, pp. 4146–4149.
- [11] Dowdeswell, J. A., Evans, S.: ‘Investigations of the form and flow of ice sheets and glaciers using radio-echo sounding’, Reports on Progress in Physics, 2004, 67, (10), pp. 1821–1861.
- [12] Burden, R. L., Faires, J. D.: ‘Solutions of Equations in one Variable’, in ‘Numerical Analysis’ (Thomson Brooks/Cole, 2005, 8th edn.), pp. 46–53.